UC San Diego
UC San Diego Previously Published Works

Title

Multiple Optimal Phenotypes Overcome Redox and Glycolytic Intermediate Metabolite Imbalances in Escherichia coli pgi Knockout Evolutions

Permalink

https://escholarship.org/uc/item/1vh7s3vn

Journal

Applied and Environmental Microbiology, 84(19)

ISSN

0099-2240

Authors

McCloskey, Douglas
Xu, Sibei
Sandberg, Troy E
et al.

Publication Date

2018-10-01

DOI

10.1128/aem.00823-18

Peer reviewed

Applied and Environmental Microbiology®

Multiple Optimal Phenotypes Overcome Redox and Glycolytic Intermediate Metabolite Imbalances in *Escherichia coli pgi* Knockout Evolutions

Douglas McCloskey,[a,b] Sibei Xu,[a] Troy E. Sandberg,[a] Elizabeth Brunk,[a] Ying Hefner,[a] Richard Szubin,[a] Adam M. Feist,[a,b] Bernhard O. Palsson[a,b]

[a]Department of Bioengineering, University of California, San Diego, La Jolla, California, USA
[b]Novo Nordisk Foundation Center for Biosustainability, Technical University of Denmark, Kongens Lyngby, Denmark

ABSTRACT A mechanistic understanding of how new phenotypes develop to overcome the loss of a gene product provides valuable insight on both the metabolic and regulatory functions of the lost gene. The *pgi* gene, whose product catalyzes the second step in glycolysis, was deleted in a growth-optimized *Escherichia coli* K-12 MG1655 strain. The initial knockout (KO) strain exhibited an 80% drop in growth rate that was largely recovered in eight replicate, but phenotypically distinct, cultures after undergoing adaptive laboratory evolution (ALE). Multi-omic data sets showed that the loss of *pgi* substantially shifted pathway usage, leading to a redox and sugar phosphate stress response. These stress responses were overcome by unique combinations of innovative mutations selected for by ALE. Thus, the coordinated mechanisms from genome to metabolome that lead to multiple optimal phenotypes after the loss of a major gene product were revealed.

IMPORTANCE A mechanistic understanding of how microbes are able to overcome the loss of a gene through regulatory and metabolic changes is not well understood. Eight independent adaptive laboratory evolution (ALE) experiments with *pgi* knockout strains resulted in eight phenotypically distinct endpoints that were able to overcome the gene loss. Utilizing multi-omics analysis, the coordinated mechanisms from genome to metabolome that lead to multiple optimal phenotypes after the loss of a major gene product were revealed.

KEYWORDS *Escherichia coli*, adaptive laboratory evolution, multi-omics analysis, mutation analysis, *pgi* gene knockout, systems biology

The flux split between upper glycolysis and the oxidative pentose phosphate pathway (oxPPP) at the glucose 6-phosphate (G6P) node is a major determinant of the flux state of a cell's core metabolic function. This is particularly true when a cell is exposed to glucose, which is commonly used is many laboratory medium formulations and is found under many environmental conditions in nature. The loss of phosphoglucose isomerase (PGI), encoded by *pgi*, induces detrimental physiological consequences (1–5). The removal of *pgi* generates an imbalance in glycolytic intermediates from the loss of upper glycolytic flux that leads to a loss of fitness and induces a sugar phosphate stress response. The sugar phosphate stress response involves the actions of both small RNAs (sRNAs) and transcription factors (TFs) that induce transcription-level changes aimed at alleviating the imbalance (6–8). The removal of *pgi* also generates an overabundance of NADPH and redox imbalance by redirecting glycolytic flux into the oxPPP. NADPH provides reducing equivalents for biosynthesis. In addition, NADPH plays an important role in reactive oxygen species (ROS) detoxification by regenerating reduced glutathione (gthrd) (9). Increased availability of NADPH in *pgi* knockout

backgrounds has proven useful in various biotechnology applications in order to increase cofactor and heterologous pathway production (1, 2, 10).

Adaptive laboratory evolution (ALE) of *pgi* mutants has been carried out to better understand the physiological changes required to overcome genetic perturbation (3, 4). ALE is an experimental method that introduces selection pressure (e.g., growth rate selection) in a controlled environmental setting (11–13). Using ALE, organisms can be perturbed from their evolutionary optimized homeostatic states, and their readjustments can be studied during the course of adaptation to reveal novel and nonintuitive component functions and interactions (14). Previous ALEs of *pgi* mutants have demonstrated a rewiring of central metabolic fluxes (4) and diversity in endpoint physiological phenotypes (3). The diversity in endpoint physiological phenotypes is directly attributed to the existence of alternate optimal metabolic and regulatory network states that can achieve the same physiological function (3). However, the mechanisms and coordination of the regulatory and metabolic network required to produce physiologically distinct, yet fit, phenotypes are not well understood. In addition, these studies were conducted with a starting strain that was not previously optimized to the growth conditions of the experiment. This confounds the interpretation of the experimental results, because adaptations to the growth conditions and loss of the gene occur simultaneously.

The consequence of the loss of a major metabolic gene can be studied at the systems level through the integration of multi-omics data sets (i.e., metabolomics, fluxomics, proteomics, and transcriptomics) to gain deeper insight into the function of the gene in the context of the biological system as a whole. Previous work has found that the metabolic network is robust to perturbations through adjustments made at the regulatory level that coordinate rerouting of flux with enzyme level (5, 15). While these studies reveal insights into the immediate response of gene loss, the adaptive changes required to overcome the loss were not explored. In addition, improvements in omics data acquisition and analysis methods could improve and reveal new relationships between changes in omics data at one layer of the system to another.

In this study, a combination of experimental design (i.e., starting with a strain that was preevolved on glucose M9 minimal medium) and systems analysis from multi-omics data was used to mechanistically investigate how multiple phenotypes can overcome the loss of *pgi*. First, the reduction in fitness after the *pgi* KO was found to be attributed to malfunctions in the regulatory and metabolic network that were incapable of handling the redox and glycolytic intermediate metabolite imbalance induced from major shifts in central metabolic flux. Second, all evolved *pgi* KO lineages regained a substantial portion of fitness but were found have mostly unique genotypes and displayed unique physiologies. Third, the recovery in fitness was enabled by mutations that were selected for by ALE that altered the transcription regulatory network (TRN) and metabolic fluxes to alleviate the redox and sugar phosphate imbalance. These regulatory and metabolic alterations were unique across all endpoints, which led to the emergence of multiple optimal phenotypes.

RESULTS

Diversity in ALE endpoint phenotypes points to multiple optimal selection outcomes. To eliminate the confounding variable of adaptation to the growth conditions of the experiment, a wild-type *E. coli* K-12 MG1655 strain previously evolved under glucose minimal medium at 37°C (16) (denoted "Ref") was selected as the starting strain (Fig. 1A). This selection was made to separate changes caused by adaptation to the loss of a gene product from those caused by adaptation to the growth conditions of the experiment.

PGI (encoded by *pgi*, phosphoglucose isomerase) was removed from the Ref strain to generate strain uPgi (for "unevolved *pgi* knockout strain") (Fig. 1B). The loss of *pgi* resulted in an 81% loss in growth rate (Fig. 1C and D). Eight uPgi independently inoculated starting cultures were simultaneously evolved on glucose minimal medium at 37°C in an automated ALE platform (16, 17) denoted "evolved *pgi* knockout strains"
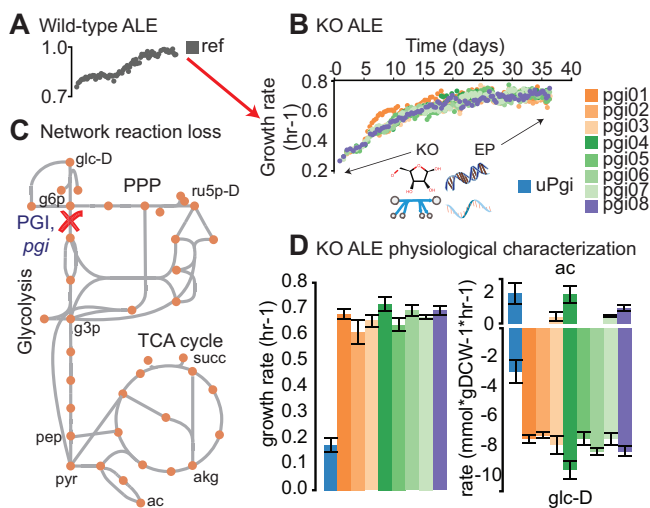
FIG 1 Evolution of knockout (KO) strains from a preevolved (i.e., optimized) wild-type strain. (A) Wild-type (wt) *E. coli* (MG1655 K-12) was previously evolved on glucose minimal medium at 37°C (16). An isolate from the endpoint of the evolutionary experiment was selected as the starting strain for subsequent KO of *pgi* and adaptive laboratory evolution (ALE). (B) Adaptive laboratory evolution trajectories of the evolved knockout lineages. Omics data were collected from the fresh KO, and endpoint lineages included metabolomics, fluxomics, physiology, DNA resequencing, and transcriptomics. (C) Phosphoglucose isomerase (PGI) was disabled by the gene KO. PGI is the first step in glycolysis and converts glucose 6-phosphate (G6P) to fructose 6-phosphate (F6P). (D) Growth rate and glucose (glc-D) uptake and acetate (ac) excretion rates for unevolved KO (uPgi) and evolved KOs (ePgi). Error bars denote 95% confidence intervals from biological triplicates. succ, succinate.

(ePgi) (Fig. 1C). A statistically significant increase in final growth rate (Student's *t* test, $P < 0.05$) was found in all ALE endpoints of the ePgi lineages (average ± standard deviation [SD], 284% ± 20% increase in growth rate) compared to the uPgi strain (Fig. 1D). Metabolomics, fluxomics, transcriptomics, genomics, and phenomics data were collected from exponentially growing cultures inoculated in triplicate from the Ref strain, the uPgi strain, and each of the 8 independently evolved endpoint lineage populations (ePgi01 to ePgi08). It is important to note that the data presented below were derived from endpoint populations as opposed to isolated clones.

Statistically significant variabilities in growth rate, acetate secretion, and glucose uptake rate were found in the ePgi samples (Fig. 1D; see also Table S1 in the supplemental material). Specifically, replicates 3, 4, 7, and 8 excreted acetate. Replicate 4, in particular, had acetate secretion levels similar to those of the uPgi strain and the highest growth and glucose consumption rates of all endpoints. The overall mutation load also differed across lineages. The overall numbers of mutations (mutation frequency, >0.2) for each of the endpoint replicates were 15, 12, 9, 13, 7, 14, 9, and 7, respectively (Table S7).

The different phenotypes and genotypes displayed by the endpoints raised two defining questions: what metabolic and regulatory changes occurred to allow for a large improvement in fitness without the use of upper glycolysis? And how were a diversity of endpoint physiologies capable of overcoming the loss of PGI? To answer these questions, intracellular metabolite levels, gene expression levels, and flux levels were measured for the Ref strain, uPgi strain, and ePgi endpoint populations (Tables S1 to S7).

PGI KO shifted metabolic flux. Genome-scale metabolic flux analysis (MFA) (18) found significant shifts in flux splits throughout central metabolism in response to the loss of PGI (Fig. 2 and Table S5). Note that all fluxes discussed in the text passed observability criteria described previously (18). Flux splits included the distribution of flux through the oxidative pentose phosphate pathway (oxPPP) (phosphogluconate dehydratase [EDD], 6-phosphogluconate dehydrogenase [GND], and 6-phosphogluconolactonase [PGL]), flux through the nonoxidative branch (nonOxPPP), flux around the anaplaerotic reactions
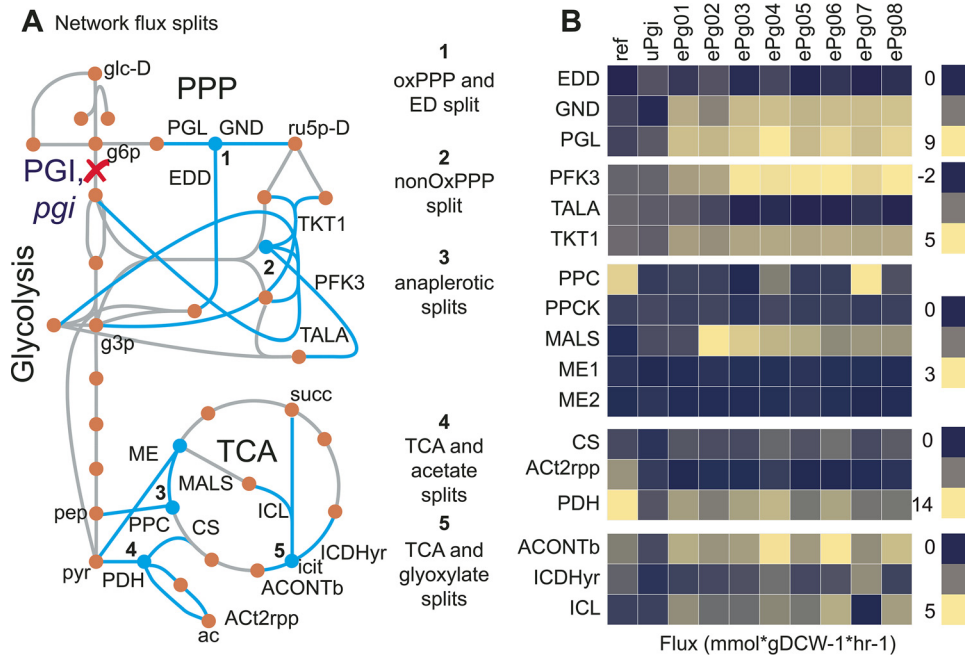
FIG 2 Changes in flux splits pre- and postadaptive evolution. (A) Network diagram with reactions involved in flux splits annotated. Reactions included phosphogluconate dehydratase (EDD), 6-phosphogluconate dehydrogenase (GND), 6-phosphogluconolactonase (PGL), phosphoenolpyruvate carboxylase (PPC), phosphoenolpyruvate carboxylase kinase (PPCK), malate dehydrogenase (MALS), NADP-dependent malic enzyme 1 (ME1), NAD-dependent malic enzyme (ME2), citrate synthase (CS), acetate secretion (ACt2rpp), pyruvate dehydrogenase (PDH), conversion of *cis*-aconitate to isocitrate (icit) carried out by the second step of the aconitase enzyme (ACONTb), isocitrate dehydrogenase (ICDHyr), and isocitrate lyase (ICL). PFK3, phosphofructokinase 3; TKT1, transketolase 1. (B) Measured absolute fluxes for the Ref strain, uPgi, and ePgi strains. Values are derived from averages taken from triplicate cultures that were analyzed in duplicate ($n = 6$).

(phosphoenolpyruvate carboxylase [PPC], phosphoenolpyruvate carboxylase kinase [PPCK], malate dehydrogenase [MALS], NADP-dependent malic enzyme 1 [ME1], and ME2), flux into the tricarboxylic acid (TCA) cycle or toward acetate secretion (citrate synthase [CS], acetate secretion [ACt2rpp], and pyruvate dehydrogenase [PDH]), and flux through the lower glyoxylate shunt or through the lower TCA cycle (aconitase [ACONTb], isocitrate dehydrogenase [ICDHyr], and isocitrate lyase [ICL]). A massive increase of over 10,000-fold in flux per mole glucose through the Entner-Doudoroff (ED) pathway (EDD) was found (note that the Ref strain had only minimal flux through the EDD), while a minor 15.6% drop in flux per mole glucose through GND was found in the uPgi strain compared to that with the Ref strain. Redistribution of flux through the nonOxPPP was found. A 79% increase in flux per mole glucose into the TCA through CS was offset by an 87% drop in flux per mole glucose into the TCA through PPC. A minor 6% drop in acetate secretion per mole glucose was found. Further, a significant 380.8% increase in flux per mole glucose through the glyoxylate shunt was found. These changes in major metabolic pathways and flux splits in the cell quantify the magnitude of the perturbation and the initial response of the cell to losing the *pgi* gene function.

Perturbed glycolytic intermediates generated a sugar phosphate stress response. Shifts in central metabolic fluxes imbalanced central metabolic intermediate metabolite levels, leading to a sugar phosphate stress response. Liquid chromatography-tandem mass spectrometry (LC-MS/MS) was used to quantify the absolute metabolite concentrations of glycolytic intermediates, pentose phosphate pathway (PPP), and TCA cycle intermediates (Table S2), and transcriptomics was used to quantify the relative shifts in genes targeted by transcription factors (Tables S2 to S4). All measured glycolytic and PPP intermediates changed significantly in the uPgi strain compared to the Ref strain (Fig. 3 and Table S2). In particular, an approximate 5-fold increase in glucose 6-phosphate (G6P) was found in the uPgi strain
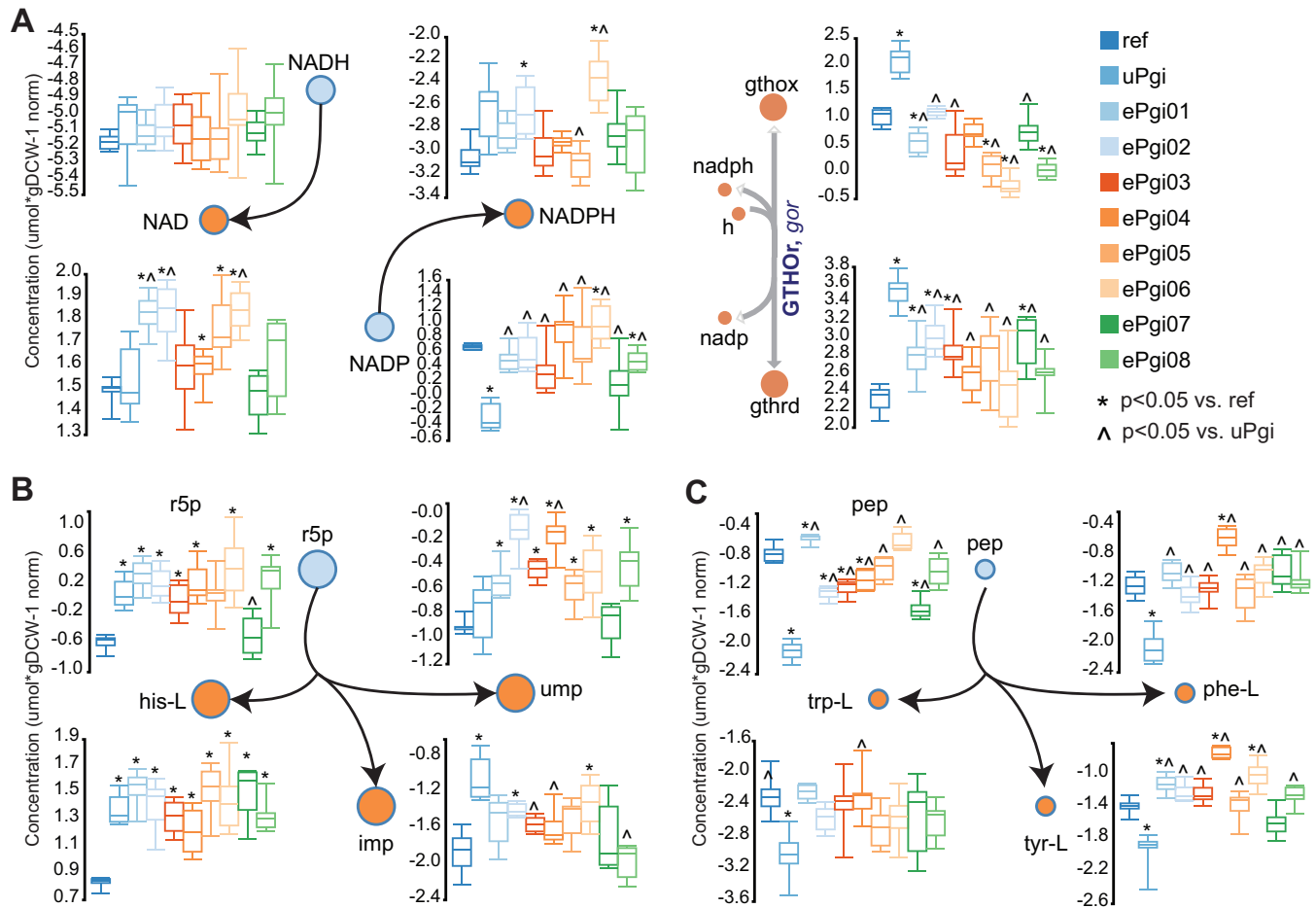
FIG 3 An imbalance in redox carriers. (A) Box-and-whisker plots of log-normalized absolute metabolite levels (μmol · gram dry cell weight [gDCW]$^{-1}$ norm) of the redox carriers NAD(P)(H) and the reduced (gthrd) and oxidized (gthox) glutathione. Network diagram of the interconversion of nadh to nad, nadp to nadph, and gthox and nadp to gthrd and nadp. An imbalance in glycolytic and PPP intermediates and their downstream biosynthetic components are shown. (B) Schematic of the connection between the PPP precursor ribose 5-phosphate (r5p) and downstream amino acid and nucleotides L-histidine (his-L), IMP, and UMP. Box-and-whisker plots of absolute metabolite levels of r5p, his-L, imp, and ump. (C) Schematic of the connection between the glycolytic precursor phosphoenol pyruvate (PEP) and downstream aromatic amino acids L-tryptophan (trp-L), L-tyrosine (tyr-L), and L-phenylalanine (phe-L). Box-and-whisker plots of PEP, trp-L, tyr-L, and phe-L. Values are derived from averages taken from triplicate cultures that were analyzed in duplicate ($n = 6$).

compared to the Ref strain (Fig. 4). G6P is the sole substrate of the *pgi* gene. Abnormal elevations in G6P and an imbalance of the glycolytic intermediates in the uPgi strain were found to induce the sugar phosphate toxicity response transcription factor (TF) SgrR (6–8), as measured through the transcriptomic measurements. SgrR is thought to bind hexose phosphates and induce the expression of the small RNA *sgrS* (6–8) (Fig. 4D and E). ePgi strains dampened *sgrS* expression, which was highly overexpressed in the uPgi strain. Further, *sgrS* transcriptionally regulates a number of genes, including the *pur* regulon, *ptsG*, and genes involved in biofilm formation and curli formation (7, 8, 19–21).

Imbalances in central carbon intermediates induced TRN responses that were consistent with the literature. Many *E. coli* TFs are activated by metabolites (22–26). Thus, changes in metabolite levels were investigated to reveal potential TRN responses as measured by changes in expression profiles associated with well-known TF regulons. Many of the measured expression changes appeared to conflict with optimal fitness. Specifically, the *glp* regulon required for glycerol import and catabolism was upregulated by C-reactive protein (CRP)-cAMP (27). cAMP was significantly elevated in the uPGI strain (supplemental material). This hard-wired regulation led to massive upregulation of the *glp* regulon in the uPgi strain, which could potentially have led to counterproductive allocation of the proteome to glycerol metabolism.
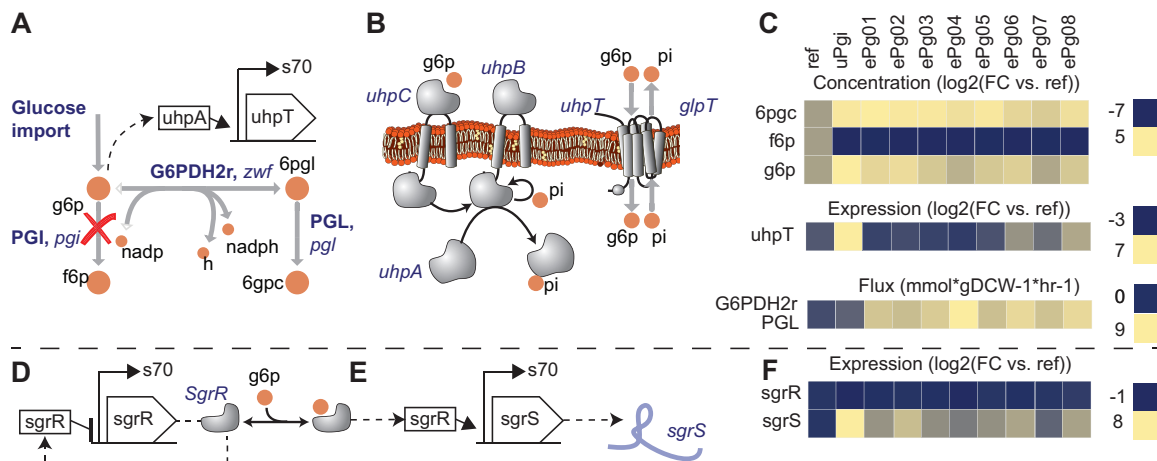
FIG 4 KO of PGI led to a hexose phosphate toxicity response. The magnitude of G6P in the initial knockout led to a deleterious cycle whereby leakage of hexose phosphate across the inner membrane (31, 32) induced hexose phosphate reuptake via the *uhpBC* two-component system and *uhpT* hexose phosphate transporter gene (28–30). (A) A network map and regulatory schematic of the reactions into and out of the G6P node. The reaction in red is removed through the PGI KO. (B) A mechanistic schematic of the *uhpBC* two-component system that sensed periplasmic hexose phosphate. The transcription factor UhpA positively upregulated the expression of the hexose phosphate importer gene *uhpT*. (C) Metabolite, expression, and flux levels near the node of perturbation. Abnormal elevations in glucose 6-phosphate (G6P) and imbalance of the glycolytic intermediates in pgi were found to induce a sugar phosphate toxicity response sensed through *sgrR* and mediated through the action of the small RNA *sgrS* (6–8) (as depicted in panels A and B). (D and E) Regulatory schematic of genes (*sgrR* and *sgrST-setA* operons) subjected to transcriptional activation or attenuation by the small RNA *sgrS* (7, 20, 74, 75). (F) Gene expression profiles of sugar phosphate response genes. Note the elevations in G6P and corresponding upregulation of *sgrS* in response to activation of SgrR by G6P that is consistent with the literature (7, 20, 74, 75). Metabolite concentrations are derived from averages taken from triplicate cultures that were analyzed in duplicate ($n = 6$). Gene expression values are derived from averages of biological duplicates.

Interestingly, the hexose phosphate importer gene, *uhpT*, was overexpressed in the uPgi strain compared to the Ref strain. High periplasmic G6P plausibly activated the *uhpAB* two-component system, which in turn upregulates the expression of the hexose phosphate importer gene *uhpT* (28–30). This result suggests that the concentration build-up in the uPgi strain was so great that G6P spilled over into the periplasmic space (31, 32) (Fig. 3, top). Increased expression of *uhpT* could have generated a loop whereby excessive G6P that spilled into the periplasmic space would be reimported into the cytosol. The transcriptional attenuation of *ptsG* by *sgrS* may act to compensate for this futile cycle.

It should be noted that in the present context, the two examples given above (i.e., the *glp* regulon and G6P cycling) could be considered counterproductive and not aligning with optimal growth. However, in a different environment, these hard-wired regulatory circuits could play a critical role in maintaining optimal physiology. This provides evidence that the combination of tightly controlled laboratory setting, gene knockout, and multi-omics data collection and analysis described here provided a useful means to reveal these hard-wired responses.

Imbalances in central carbon intermediates were mirrored in amino acid pools. In addition to regulatory shifts, biomass components directly reflected the levels of their biosynthetic precursors (Fig. 3B and C). The aromatic amino acids L-tyrosine (tyr-L), L-phenylalanine (phe-L), and L-tryptophan (trp-L) are derived from phosphoenolpyruvate (PEP). A decrease in PEP levels in the uPgi strain and a rise in PEP levels in the ePgi strains were mirrored by all three of the amino acids (Fig. 3C). An increase in ribose 5-phosphate (r5p) levels in the uPgi and ePgi strains were mirrored by the downstream amino acid L-histidine (his-L) and nucleotide UMP (Fig. 3B).

Similar trends were found for amino acid and precursor pairs L-serine (ser-L) and 2-phosphogluconate (2pg), L-aspartate (asp-L) and oxaloacetate (oaa), L-alanine (ala-L) and pyruvate (pyr), and L-glutamate (glu-L), L-glutamine (glu-L), and alpha-ketoglutarate (akg), respectively (Table S2). Perturbations in the distribution and abundance of proteogenic amino acids have been shown to alter protein synthesis rates, leading to
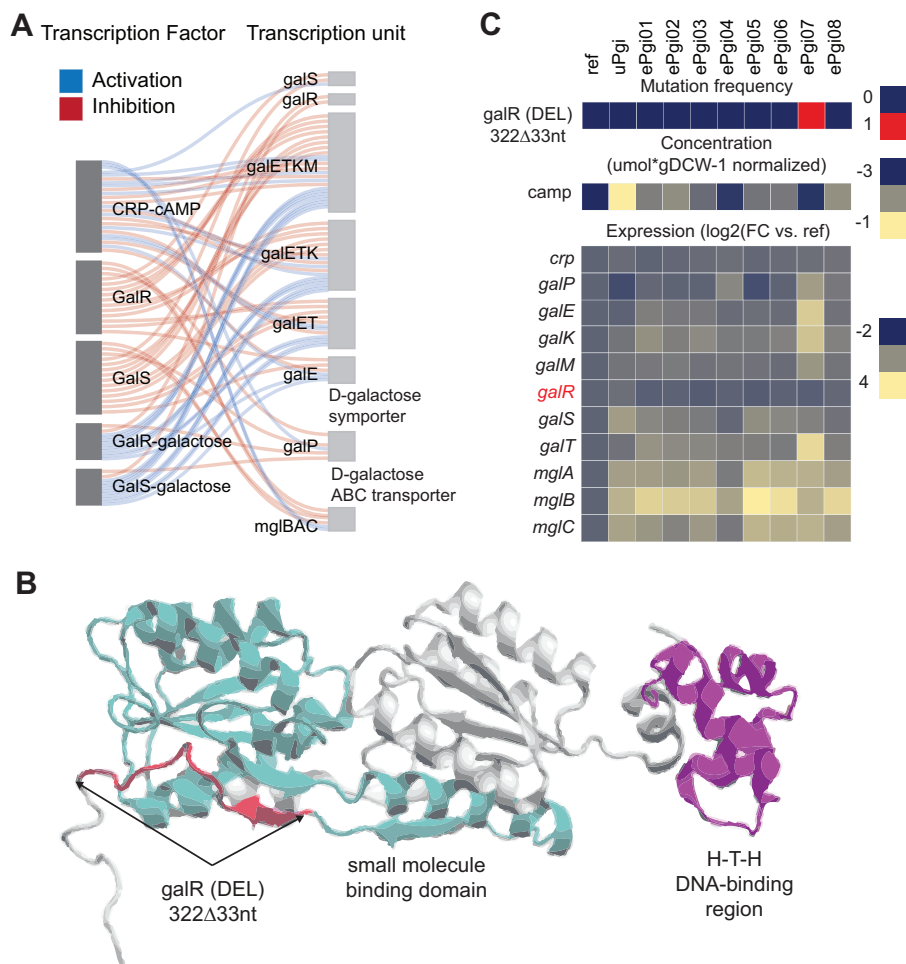
FIG 5 An in-frame 33-nucleotide deletion (DEL) that removed 11 amino acids in the small-molecule-binding domain of *galR* negates *galR* repression in ePgi07. (A) Regulatory network specifically controlled by cAMP-CRP, *galR*, and *galS* (76–78). cAMP-CRP can both positively and negatively regulate the expression of *galR*, *galS*, *galETKM*, *galP*, and *mglBAC*; GalR and GalS act as repressors; and GalR and GalS bound to galactose active primarily as activators. (B) Crystal structure of the *galR* transcription factor (70). The position of the deletion is highlighted in red, the small-molecule-binding domain is highlighted in cyan, and the H-T-H DNA-binding region is highlighted in magenta. Images created using the VMD software tool (v. 1.9.2; http://www.ks.uiuc.edu/Research/vmd/). (C) Mutation frequency for *galR*, metabolite concentration for cAMP, and expression profiles of *galR*-controlled operons. Note the increased expression of *galP* and *galETKM* in ePgi07. Metabolite concentrations are derived from averages taken from triplicate cultures that were analyzed in duplicate ($n = 6$). Gene expression values are derived from averages of biological duplicates.

a drop in the growth rate (33–37). The drop in the growth rate of the uPgi strain and regain of fitness in the ePgi strains provide evidence that an imbalance in glycolytic intermediates directly alters growth rate via manipulating proteogenic amino acid levels.

The regulatory response to elevated G6P levels and the relationship between biomass components and their precursors reflected the importance of balancing glycolytic, PPP, and TCA cycle intermediates to maintain balanced ratios of amino acid levels for protein biosynthesis and purine/pyrimidine mononucleotides for nucleotide biosynthesis.

Mutations that targeted alternative glucose import systems corrected TRN responses and helped rebalance glycolytic intermediate levels. Major alterations in expression profiles were found in the evolved KO strains that correlated well with mutations detected in TFs. These included mutations to *galR* (Fig. 5) and *malT* (Fig. 6) in the ePgi strains. A 22-nucleotide deletion in the small-molecule-binding domain of
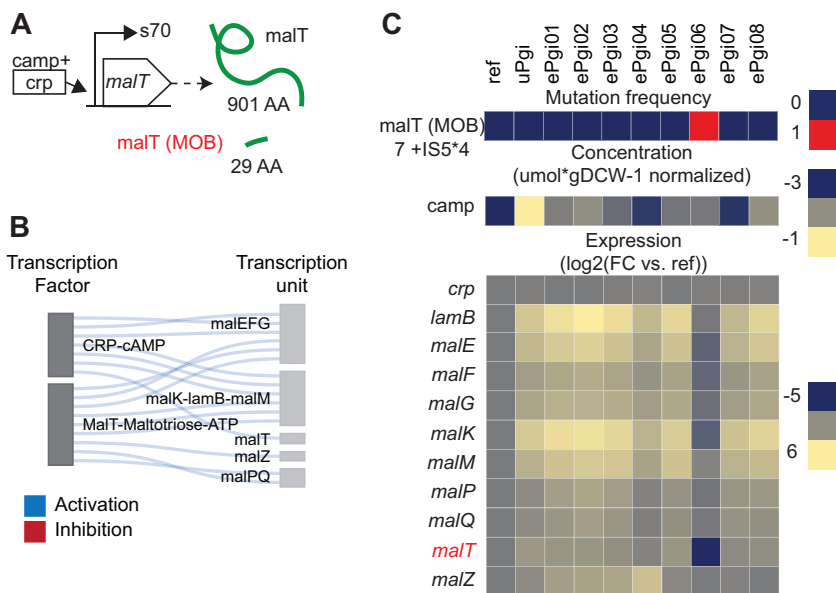
FIG 6 A mobile element insertion (MOB) that truncated the MalT TF in ePgi06 was found that appeared to silence the expression of MalT-controlled operons. (A) Schematic of the *malT* operon (39) and truncated MalT peptide. The mobile element insertion introduced a stop codon that reduced the MalT peptide from 901 amino acids to 29 amino acids. All binding domains and catalytic sites were cleaved (40, 41). (B) Operons controlled by *malT* (39). All regulators except *malT* and CRP-cAMP have been omitted. MalT-controlled genes are involved in glycogen turnover and may give ePgi06 an advantage in controlling the levels of hexose phosphates that are converted to and broken down from glycogen. (C) Mutation frequency of *malT*, metabolite concentration for cAMP, and expression profiles for *malT* and *malT*-regulated genes. Note the significantly repressed gene expression levels of MalT-controlled genes in ePgi06. Metabolite concentrations are derived from averages taken from triplicate cultures that were analyzed in duplicate (*n* = 6). Gene expression values are derived from averages of biological duplicates.

galR in ePgi07 appears to negate the repression of the *galR*-controlled operons (Fig. 5). These include *galETKM*, *galP*, and *mglBAC* that encode enzymes for galactose catabolism, symport, and ABC transport, respectively (38). These operons are also regulated by CRP-cAMP and were not expressed in the Ref strain. The galactose importers have lesser affinity for the transport of glucose, which may give ePgi07 an additional route to import and catabolize glucose from the environment. In addition, the mutation may have aided in conserving PEP for aromatic amino acid production, which was limiting fitness in all of the *pgi* strains (as discussed previously).

In another example, a mobile element insertion (MOB) that truncated the MalT TF in ePgi06 was found that appeared to silence the expression of operons controlled by MalT (39) (Fig. 6). The MOB introduced a stop codon that truncated the MalT peptide from 901 amino acids to 29 amino acids. All binding domains and catalytic sites were cleaved (40, 41). MalT-controlled genes are involved in glycogen turnover and may give ePgi06 an advantage in controlling the levels of hexose phosphates that are converted to and broken down from glycogen.

An imbalance in redox carriers was compensated for by shifts in hydrogenase flux and buffered by glutathione. Genome-scale MFA (18) confirmed that removal of the *pgi* gene diverted all upper glycolytic flux into the oxidative pentose phosphate pathway (oxPPP) (Fig. 2). The loss of PGI resulted in a 556.7% increase in flux per mole glucose toward the oxPPP in the uPgi strain (14.4 and 94.7% flux per mole glucose in the Ref and uPgi strains, respectively). Note that as discussed previously, a large portion of the flux into the oxPPP was diverted down the ED pathway after the first NADPH-generating step to avoid generating additional NADPH via the second NADPH-generating step of the oxPPP (Fig. 2). Rearrangement of flux through hydrogenases to compensate for the increased flux toward NADPH generation were found (Fig. 2). Notable is the reversed utilization of the transhydrogenases from net NADPH to NADH

generation in the uPgi and ePgi strains (approximately −8-fold change in the uPgi and ePgi strains in NADPH generation through pyridine nucleotide transhydrogenase [THD2pp], and −3-fold change in the uPgi strain and −1 to 4-fold change in ePgi strains in NADH generation through pyridine nucleotide transhydrogenase [NADTRHD]). Other hydrogenases significantly altered include serine dehydrogenase (LSERDHr, note the altered levels of ser-L mentioned previously), as well as isocitrate dehydrogenase (ICD) and glutamate synthase (GLUSy, note the altered levels of akg, gln-L, and glu-L mentioned previously).

The increased flux through the oxPPP would generate an increased abundance of NADPH and thus a redox imbalance. LC-MS/MS (42) was used to quantify the absolute metabolite concentrations of the redox carriers. While major shifts in the redox carriers were found (Fig. 3A), a statistically significant change in NADPH between the Ref and uPgi strains was not found. However, statistically significant changes in NADP and reduced and oxidized glutathione were found. This indicates a potential rapid buffering of NADPH by the glutathione via glutathione reductase (GTHOr) (Fig. 3A).

High NADPH promoted activation of oxidative stress responders. Mutations in *soxR* in ePgi02 and *rseC* in ePgi01 were found that altered the expression of oxidative stress genes (Fig. 7). The *soxR* mutation truncated the Fe-S cluster binding site of the SoxR peptide by introducing a premature stop codon (Fig. 7C). Cleavage of the Fe-S cluster does not affect DNA binding, but transcriptional activation of the target genes *soxS* and *fumC* and transcriptional deactivation of *soxR* are impaired (43–45). *soxR* was upregulated in ePgi02, which indicated that the mutation negated the self-regulation of *soxR*.

The *rseC* single-nucleotide deletion introduced a frameshift that truncated a large portion of the transmembrane helix region starting several amino acids from the initial deletion (Fig. 7D) that may affect Rsx-RseC complex formation or activity. *rseC* mutants were found previously to exhibit constitutive *soxS* expression by preventing the Rsx-RseC complex from inhibiting reduction and inactivating SoxR (46) (Fig. 7A). *soxS*, as well as many of its downstream activation targets, including *acrA*, *acrB*, *fldA*, *fpr*, *inaA*, and *sodA*, were upregulated in ePgi01, which indicated that the mutation promotes the expression of *soxS*. The Rsx-RseC complex prevents the reduction and inactivation of SoxR (46).

Mutations in transhydrogenases helped alleviate redox imbalance. Mutations selected during adaptive evolution also introduced innovations that targeted metabolic network elements involved in NADPH production. Mutated transhydrogenases included *sthA*, *pntB*, *icd*, and *zwf*. The soluble and membrane-bound transhydrogenases act to interconvert NADP(H) and NAD(H) (47, 48) (Fig. 8). Mutations in the soluble *sthA* (50) and membrane-bound *pntB* (51) transhydrogenase genes in ePgi07 and ePgi04, respectively, were found (Fig. 8). The *sthA* mutation appeared near the dimerization domain and may affect enzyme complex formation. The *pntB* mutation appeared in the transmembrane region and may affect catalytic activity or membrane association. It has been demonstrated that altered activities of *sthA* and *pntAB* confer a fitness advantage in *pgi* mutant strains by rebalancing the ratio of NADH to NADPH (47, 48). Interestingly, mutations in *sthA* and *pntB* were selected for in previous evolutions of a *pgi* strain (3). This observation provides further evidence that the *sthA* and *pntB* mutations provided a fitness advantage to ePgi07 and ePgi04 by rebalancing the ratios of NADH to NADPH via modulating the activities of the transhydrogenases. Note that ePgi07 and ePgi04 were also found to have the highest increases in flux through the soluble transhydrogenases.

Isocitrate dehydrogenase (ICD) catalyzes the conversion of isocitrate (icit) to 2-oxoglutarate (akg) while reducing $NADP^+$ to NADPH (Fig. 9). The activity of ICD also regulates the flux split between the full TCA cycle and the glyoxylate shunt (49–51). A point mutation at residue 395 that changed the amino acid from positively charged (L-arginine) to negatively charged (L-cysteine) in ICD was found in all ePgi replicates except replicate 7 (Fig. 9). The mutation occurs 4 Å from the phosphate moiety of
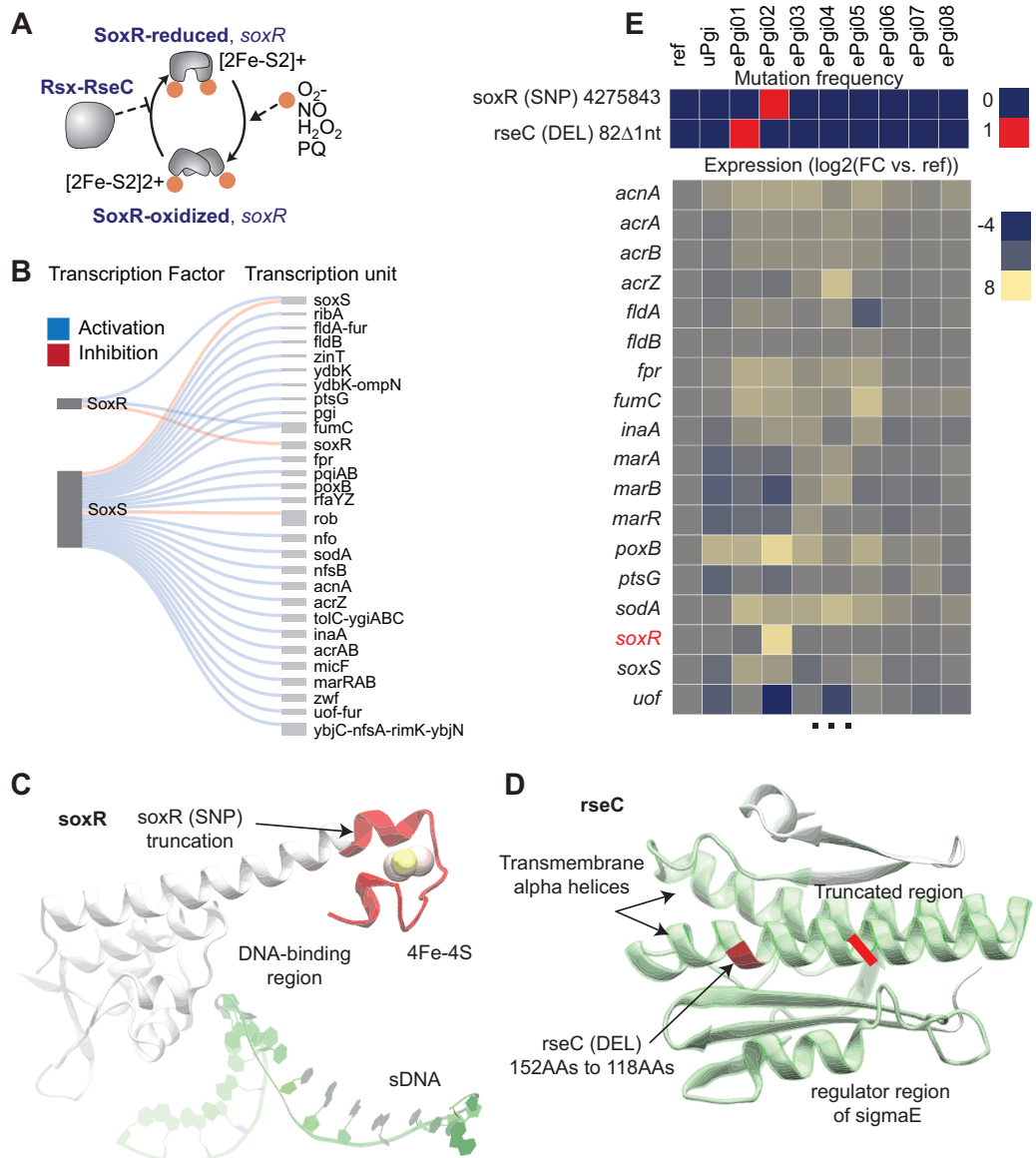
FIG 7 Mutations in *soxR* and *rseC* that altered the expression of oxidative stress genes. (A) Protein-protein interaction schema between SoxR and Rsx-RseC. In the reduced form, the iron sulfur clusters of the SoxR homodimers sense the presence of free radicals and ROS (79, 80). The oxidation of the iron sulfur clusters by free radicals and ROS induces a conformation changes from the inactive form to the active form (81). While both reduced and inactive forms and oxidized and active forms of SoxR are capable of binding DNA, only the active form is capable of activating or inhibiting transcription (43, 82–85). The Rsx-RseC complex prevents reduction and inactivation of SoxR (46). (B) Regulatory schematic of a subset of SoxR and SoxS-controlled operons. (C) Crystal structure of SoxR (86). The *soxR* single-nucleotide polymorphism (SNP) eliminated the Fe-S cluster binding site of the SoxR peptide. The SoxR DNA-binding region in proximity to single-stranded DNA (sDNA) is shown below. (D) Crystal structure of *rseC*. The *rseC* mutation cleaved a large portion of the transmembrane helix region that may affect Rsx-RseC complex formation or activity. The mutated and/or cleaved residues are shown in red. AAs, amino acids. Images in panels C and D were created using the VMD software tool (v. 1.9.2; http://www.ks.uiuc.edu/Research/vmd/). (E) Mutation frequency and gene expression profiles. Gene expression values are derived from averages of biological duplicates.
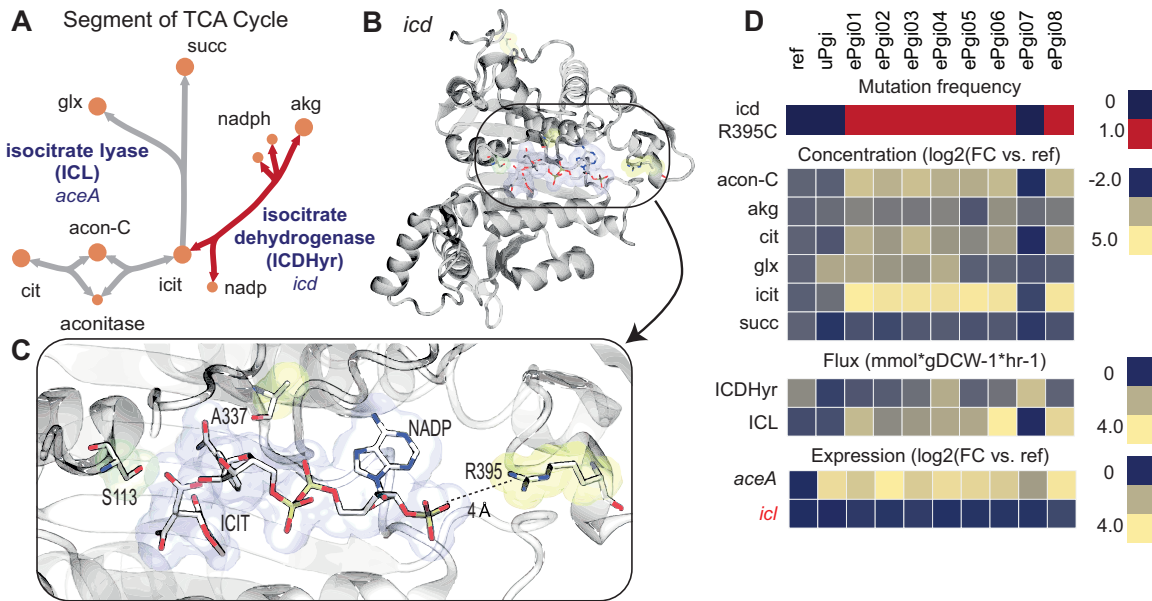
NADP. Residue 395 has been shown to be directly involved in NADP binding (52) and appears to allow the mutated enzyme to either utilize NAD as a cofactor or exclude NADPH from the active site by like-charge repulsion. The mutation was found to redirect flux through the glyoxylate shunt instead of the TCA cycle and may provide a fitness advantage to the ePgi strains by limiting the production of NADPH in the TCA cycle.

The metabolome, fluxome, transcriptome, and genome were unique in each ePgi strain. While the ePgi strains were not able to recover the fitness of the Ref strain,
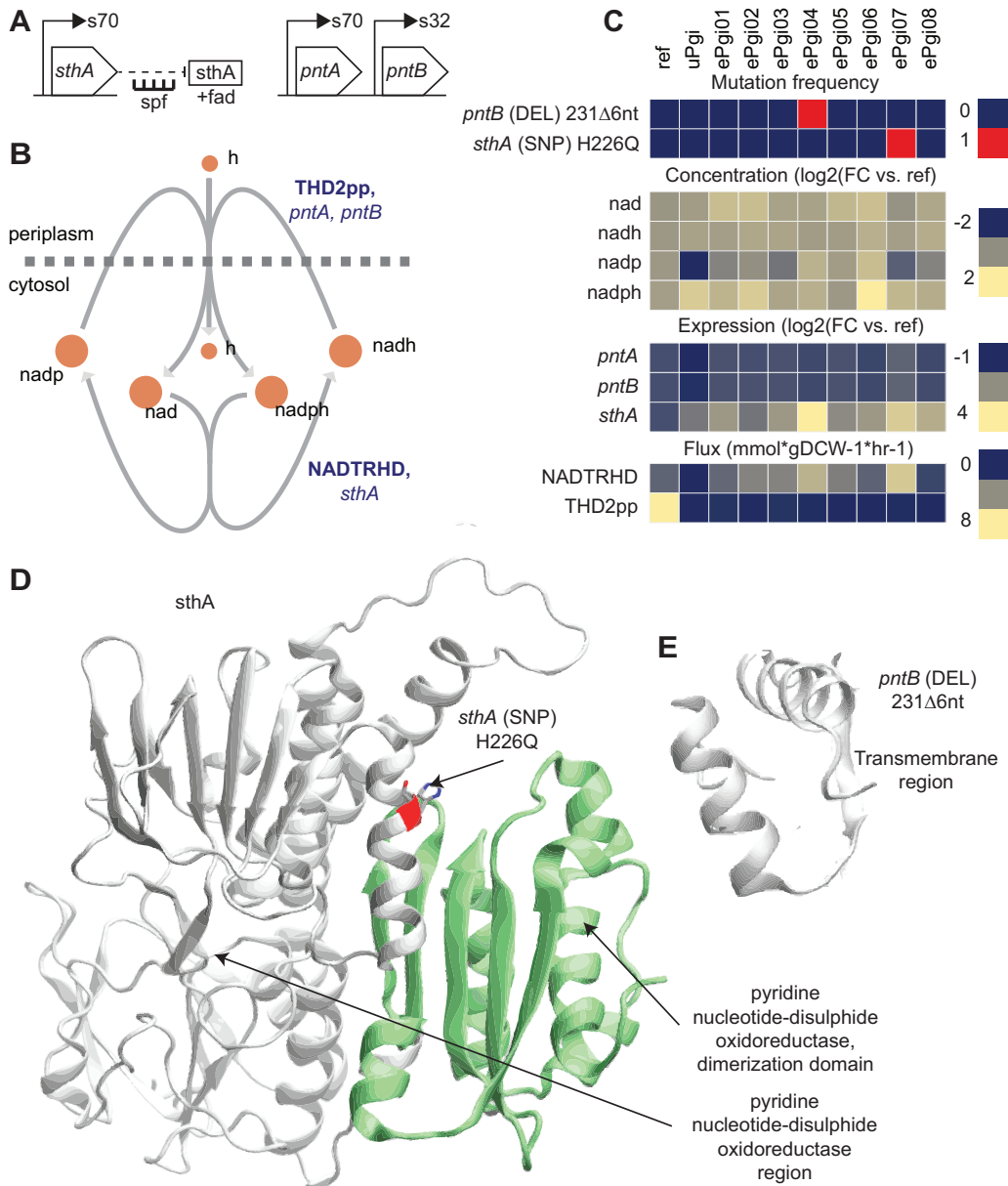
FIG 8 Mutations in the soluble *sthA* (50) and membrane-bound *pntB* (51) transhydrogenases that potentially aid in balancing NAD(P)(H) cofactors. (A) Schematic of the *sthA* and *pntAB* operons. (B) Network diagrams of the soluble pyridine nucleotide transhydrogenase (NADTRHD) reaction catalyzed by *sthA* and the membrane-bound pyridine nucleotide transhydrogenase (THD2pp) reaction catalyzed by *pntAB*. (C) Mutation frequency and metabolite and expression levels near the genes. (D) The *sthA* mutation in ePgi04 appeared near the dimerization domain and may affect enzyme complex formation. (E) The *pntB* mutation in ePgi07 appeared in the transmembrane region and may affect catalytic activity or membrane association. It has been demonstrated that the altered activities of *sthA* and *pntAB* confer a fitness advantage in *pgi* mutant strains by rebalancing the ratios of NADH to NADPH (47, 48). Metabolite concentrations are derived from averages taken from triplicate cultures that were analyzed in duplicate (*n* = 6). Gene expression values are derived from averages of biological duplicates. Images in panels D and E were created using the VMD software tool (v. 1.9.2; http://www.ks.uiuc.edu/Research/vmd/).

they were able to recover the initial growth rate of wild-type MG1655. Many intermediate and cofactor levels, including G6P, remained perturbed in ePgi strains to various degrees. However, the majority of initially elevated transcription involving sugar phosphate stress, carbon catabolite repression, the *uhpT* transporter, and other general stress responders in the uPgi strain were dampened or completely shut down in ePgi strains. This indicated that the TRN had evolved to cope with the changed metabolome. Many of these changes to the TRN could be directly attributed to mutations.

FIG 9 A beneficial mutation that rewired the TCA cycle via a cofactor usage swap in isocitrate dehydrogenase (ICD) aided in alleviating the excessive conversion of NADP to NADPH. (A) Network schematic of a segment of the TCA cycle. The reaction in red is catalyzed by ICD. (B) Crystal structure of ICD. The mutated amino acids are highlighted in yellow. (C) Zoom-in on the active site of isocitrate dehydrogenase showing the proximity of the mutated amino acid to the phosphate group of NADP. The mutation occurs 4 Å from the phosphate moiety of NADPH. Residue 395 has been shown to be directly involved in NADPH binding (52) and appears to allow the mutated enzyme to utilize NADH as a cofactor. Images in panels B and C were created using the VMD software tool (v. 1.9.2; http://www.ks.uiuc.edu/Research/vmd/). (D) Mutation frequency and metabolite, expression, and flux levels near the mutated gene. System components near the ICDHyr reaction in the ICD mutant strains are significantly changed. Metabolite concentrations are derived from averages taken from triplicate cultures that were analyzed in duplicate ($n = 6$). Flux levels are derived from averages taken from triplicate cultures that were analyzed in duplicate ($n = 6$). Gene expression values are derived from averages of biological duplicates.

The recovery to wild-type levels was in part made possible by a complete rewiring of central carbohydrate metabolic flux splits (Fig. 3). The rewiring differed substantially between ePgi strains. While an increase in flux through GND and a decrease in flux through the ED pathway occurred in all ePgi endpoints, the flux through each pathway differed substantially. GND flux increases varied from 389.9 to 604.6% per mole glucose compared to the Ref strain, and ED pathway flux increases varied from 150.9 to 4,463.8% per mole glucose compared to the Ref strain. nonOxPPP flux varied substantially among the strains, even altering between net forward and reverse utilization of transaldolase A (TALA). Of particular note, flux through PPC was regained in ePgi04 and ePgi07, and flux through the glyoxylate shunt was lost in ePgi07. The increased flux through the PPC and loss of flux through the glyoxylate shunt in particular correlate with mutations in the transhydrogenases and *icd*, respectively.

Conclusion. The loss of *pgi* induced massive perturbations to the metabolome, fluxome, and transcriptome in *E. coli* and led to a greatly retarded postknockout growth rate. In contrast to previous work (5), it was found that the loss of *pgi* induced major changes in all omics data measured not just local to the perturbation but also in distal network locations. Flux rerouting to compensate for the loss of *pgi* imbalanced the PPP and glycolytic intermediate levels, which led to a sugar phosphate stress response. The deleterious effects of this response were attributed to a misallocation of protein, a deleterious cycle of reimport of hexose phosphate, and alterations in the distributions and amount of proteogenic amino acids and nucleotides. Redistribution of glycolytic flux into the oxPPP generated an overabundance of NADPH, which led to a redox imbalance.

ALE selected for mutations that helped alleviate redox and glycolytic intermediate imbalances. Differences in the metabolome and mutation landscape led to a diversity of expression and fluxome profiles in ePgi strains. The multitude of hydrogenases and routes to generate glycolytic intermediates allowed for regulatory and metabolic

TABLE 1 Primers used to generate the *pgi* KO strains in this study

			Confirmation	
Primer	Name	Sequence	Name	Sequence
F_KO_primer	pgi_F_KO_primer	ACAATTCTCAAAATCAGAAGAGTATTGCTAATGAAAAACATCAATCCAACGCAGACCGCTATTCCGGGGATCCGTCGACC	F_conf_pr	AGCGGGGCGGTTGTCAACGA
R_KO_primer	pgi_R_KO_primer	CGCCTTATCCGGCCTACATATCGACGATGATTAACCGCGCCACGCTTTATAGCGGTTAATGTGTAGGCTGGAGCTGCTTC	R_conf_pr	TTTATCTGATAAAAAAATGC

flexibility in overcoming redox and glycolytic intermediate imbalance. Finally, the diversity in fixed mutations and the concomitant emergence of multiple optimal phenotypes was a manifestation of this metabolic flexibility. Additional studies utilizing ALE to uncover the response of a cell to a major network perturbation are likely to uncover additional mechanisms available to biological networks to overcome such major perturbations.

MATERIALS AND METHODS

Biological material, analytical reagents, and experimental conditions. (i) Biological material. A wild-type *E. coli* K-12 MG1655 strain previously evolved under glucose minimal medium at 37°C (ATCC 700926) (16, 17) served as the starting strain. Lambda Red-mediated DNA mutagenesis (53) was used to create the knockout strains (DNA mutagenesis and PCR confirmation primers are given in Table 1,). Knockouts were confirmed by PCR and DNA resequencing. The *pgi* gene encoding triphosphate isomerase (TPI) was removed. All cultures were grown in 25 ml of unlabeled or labeled glucose M9 minimal medium (54) with trace elements (55) and sampled from a heat block in 50-ml autoclaved tubes that were maintained at 37°C and aerated using magnetics.

(ii) Materials and reagents. Uniformly labeled [^{13}C]glucose and 1-[^{13}C]glucose was purchased from Cambridge Isotope Laboratories, Inc. (Tewksbury, MA). Unlabeled glucose and other medium components were purchased from Sigma-Aldrich (St. Louis, MO). LC-MS reagents were purchased from Honeywell Burdick & Jackson (Muskegon, MI), Fisher Scientific (Pittsburgh, PA), and Sigma-Aldrich.

(iii) Reaction knockout selection. iJO1366 (56) was used as the metabolic model for *E. coli* metabolism; GLPK (version 4.57) was used as the linear program solver. Markov chain Monte Carlo (MCMC) sampling (57) was used to predict the flux distribution of the optimized reference strain. Uptake, secretion, and growth rates were constrained to the measured average value $\pm$ the SD. Potential reaction deletions were ranked by (i) averaged sampled flux, (ii) the number of immediate upstream and downstream metabolites that could be measured, and (iii) the number of genes required to produce a functional enzyme. The reactions involved in sampling loops that were spontaneous, computationally or experimentally essential, or not actively expressed under the experimental growth conditions were not included in the analysis. Also, reactions that would require more than one genetic alteration to abolish activity were excluded. The top 9 reaction deletions from the rank-ordered set of reactions that met the above-mentioned criteria were chosen for implementation.

Adaptive laboratory evolution. Cultures were serially propagated (100 μl passage volume) in 15-ml (working volume) flasks of M9 minimal medium with 4 g/liter glucose, kept at 37°C, and well mixed for full aeration. An automated system passed the cultures to fresh flasks once they had reached an optical density at 600 nm (OD$_{600}$) of 0.3 (equivalent to an OD$_{600}$ of ~1 on a traditional spectrophotometer with a 1-cm path length; Tecan Sunrise plate reader), a point at which nutrients were still in excess and exponential growth had not started to taper off (confirmed with growth curves and high-performance liquid chromatography [HPLC] measurements). Four OD$_{600}$ measurements were taken from each flask, and the slope of ln(OD$_{600}$) versus time determined the culture growth rates. A cubic interpolating spline constrained to be monotonically increasing was fit to these growth rates to obtain the fitness trajectory curves.

Multi-omics data processing. (i) Phenomics. Physiological measurements for culture density were measured at 600 nm absorbance with a spectrophotometer and correlated to cell biomass. Samples to determine substrate uptake and secretion were filtered through a 0.22-μm filter (polyvinylidene difluoride [PVDF]; Millipore) and measured using refractive index (RI) detection by HPLC (Agilent 12600 Infinity) with a Bio-Rad Aminex HPX87-H ion exclusion column (injection volume, 10 μl) and 5 mM H$_2$SO$_4$ as the mobile phase (0.5 ml/min, 45°C). Growth, uptake, and secretion rates were calculated from a minimum of four steady-state time points.

(ii) LC-MS/MS instrumentation and data processing. Metabolites were acquired and quantified on Qtrap 5500 mass spectrometer (AB Sciex, Framingham, MA) and processed using MultiQuant 3.0.1, as described previously (42). Mass isotopomer distributions (MIDs) were acquired on the same instrument and processed using MultiQuant 3.0.1 and PeakView 2.2, as described previously (58).

(iii) Metabolomics. Internal standards were generated as described previously (59). All samples and calibrators were spiked with the same amount of internal standard taken from the same batch of internal standards. Calibration curves were run before and after all biological and analytical replicates. The consistency of quantification between calibration curves was checked by running a quality control sample that was composed of all biological replicates twice a day. Solvent blanks were injected every

ninth sample to check for carryover. System suitability tests were injected daily to check instrument performance.

Metabolomics samples were acquired from triplicate cultures (1 ml of cell broth at an OD$_{600}$ of ~1.0) using a previously described method (60). A pooled sample of the filtered medium that was resampled using the fast Swinnex filtration (FSF) technique and processed in the same way as the biological triplicates was used as an analytical blank. Extracts obtained from triplicate cultures and refiltered medium were analyzed in duplicate. The intracellular values reported, unless otherwise noted, are derived from the average of the biological triplicates ($n = 6$). Metabolites in the pooled filtered medium with a concentration greater than 80% of that found in the triplicate samples were not analyzed. In addition, metabolites that were found to have a quantifiable variability (relative standard deviation [RSD], $\geq$50%) in the quality control samples or any individual components with an RSD of $\geq$80 were not used for analysis.

Missing values were imputed using a bootstrapping approach, as coded in the R package Amelia II (version 1.7.4, 1,000 imputations) (61). The remaining missing values were approximated as $^1/_2$ the lower limit of quantification for the metabolite normalized to the biomass of the sample. Prior to statistical analyses, metabolite concentrations were log normalized to generate an approximately normal distribution using the R package LMGene (62) (version 3.3, "mult" = "TRUE," "lowessnorm" = "FALSE"). A Bonferroni-adjusted P value cutoff of 0.01, as calculated from Student's t test, was used to determine significance between metabolite concentration levels. The glog-normalized values or the median-normalized values to the reference strain (fold change [FC] of the median versus the Ref strain) were used for downstream statistical analyses.

(iv) Fluxomics. Fluxomics samples were acquired from triplicate cultures (10 ml of cell broth at an OD$_{600}$ of ~1.0) using a modified version of the FSF technique, as described previously (58). MIDs were calculated from biological triplicates run in analytical duplicates ($n = 6$). MIDs with an RSD greater than 50% were excluded. In addition, MIDs with a mass that was found to have a signal greater than 80% in unlabeled or blank samples were excluded. A previously validated genome-scale MFA model of *E. coli* with minimal alterations was used for all MFA estimations using INCA (version 1.4) (63), as described previously (18). The model was constrained using MIDs, as well as measured growth, uptake, and secretion rates. Best flux values that were used to calculate the 95% confidence intervals were estimated from 500 restarts.

The 95% confidence intervals were used as lower and upper bound reaction constraints for further constraint-based analyses. MFA-derived constraints that violated optimality were discarded and resampled. The descriptive statistics (i.e., mean, median, interquartile ranges, minimum, maximum, etc.) for each reaction for each model were calculated from 5,000 points sampled from 5,000 steps using optGpSampler (version 1.1) (64), which resulted in an approximate mixed fraction of 0.5 for all models. A permuted P value of <0.05 and geometric fold change of sampled flux values of >0.001 were used to determine differential flux levels, differential metabolite utilization levels, and differential subsystem utilization levels between models. Demand reactions and reactions corresponding to unassigned, transport; outer membrane porin, transport; inner membrane, inorganic ion transport and metabolism, transport; and outer membrane, nucleotide salvage pathway, oxidative phosphorylation were excluded from differential flux analysis. The geometric fold change of the mean between models and the reference model was used for hierarchical clustering; the median, interquartile ranges, minimum, and maximum values of each sampling distribution for each reaction and model were used as representative samples for downstream statistical analyses.

(v) Transcriptomics. Total RNA was sampled from triplicate cultures (3 ml of cell broth at an OD$_{600}$ of ~1.0), immediately added to 2 volumes of Qiagen RNAprotect bacteria reagent (6 ml), vortexed for 5 s, incubated at room temperature for 5 min, and immediately centrifuged for 10 min at 17,500 rpm. The supernatant was decanted, and the cell pellet was stored at −80°C. Cell pellets were thawed and incubated with Ready-Lyse lysozyme, SUPERaseIn, protease K, and 20% SDS for 20 min at 37°C. Total RNA was isolated and purified using the Qiagen RNeasy minikit columns and following vendor procedures. An on-column DNase treatment was performed for 30 min at room temperature. RNA was quantified using a NanoDrop spectrophotometer and assessed for quality by running an RNA Nano chip on a Bioanalyzer. The rRNA was removed using Epicentre's Ribo-Zero rRNA removal kit for Gram-negative bacteria. A Stranded RNA sequencing (RNA-Seq) kit (catalog no. KK8401; Kapa Biosystems) was used, according to the manufacturer's protocol, to create sequencing libraries with an average insert length of around ~300 bp for two of the three biological replicates. Libraries were run on a MiSeq and/or HiSeq platform (Illumina).

RNA-Seq reads were aligned using Bowtie (version 1.1.2, with default parameters) (65). Expression levels for individual samples were quantified using Cufflinks (version 2.2.1, library type fr-firststrand) (66). The quality of the reads was assessed by tracking the percentage of unmapped reads and expression level of genes that mapped to the ribosomal gene loci *rrsA* to *rrsF* and *rrlA* to *rrlF*. All samples had a percentage of unmapped reads of less than 7%. Differential expression levels for each condition ($n = 2$ per condition) compared to either the starting strain or initial knockout strain were calculated using Cuffdiff (version 2.2.1, library type fr-firststrand, library norm geometric) (66). Genes with a 0.05 false-discovery rate (FDR)-adjusted P value of <0.01 were considered differentially expressed. The expression levels for individual samples for all combinations of conditions tested in downstream statistical analyses were normalized using Cuffnorm (version 2.2.1, library type fr-firststrand, library norm geometric) (66). Genes with unmapped reads were imputed using a bootstrapping approach as coded in the R package Amelia II (version 1.7.4, 1,000 imputations). The remaining missing values were filled using the minimum expression level of the data set. Normalized fragments per kilobase per million (FPKM) values for gene expression were log$_2$ normalized to generate an approximately normal distribution prior to any statistical analysis. All replicates for a given condition were found to have a pairwise Pearson correlation coefficient of 0.95 or greater.

(vi) DNA resequencing. Total DNA was sample from an overnight culture (1 ml of cell broth at an OD_{600} of ~2.0) and immediately centrifuged for 5 min at 8,000 rpm. The supernatant was decanted, and the cell pellet was frozen at −80°C. Genomic DNA was isolated using a NucleoSpin tissue kit (catalog no. 740952.50; Macherey-Nagel), according to the manufacturer's protocol, including treatment with RNase A. Resequencing libraries were prepared using a Nextera XT kit (catalog no. FC-131-1024; Illumina), following the manufacturer's protocol. Libraries were run on a MiSeq platform (Illumina). DNA resequencing reads were aligned to the *E. coli* reference genome (GenBank accession no. U00096.2) using breseq (version 0.26.0) (67) as populations. Mutations with a frequency of less than 0.1, *P* value greater than 0.01, or quality score less than 6.0 were removed from the analysis. In addition, genes corresponding to *crl*, insertion elements (i.e., *insH1*, *insB1*, and *insA*), and the *rhs* and *rsx* gene loci were not considered for analysis due to repetitive regions that appear to cause frequent miscalls when using breseq. mRNA and peptide sequence changes were predicted using BioPython (https://github .com/biopython/biopython.github.io/). Large regions of DNA (minimum of 200 consecutive indices) where the coverage was two times greater than the average coverage of the sample were considered duplications.

Structural analysis. Corresponding Protein Data Bank (PDB) files for genes with a mutation of interest were downloaded from PDB (68, 69). Structural models for genes for which there were no corresponding PDB files were taken from I-TASSER-generated homology models (70) or generated using the I-TASSER protocol (71). The BioPython-predicted sequence changes and important protein features as listed in EcoCyc (72) were visualized and annotated using VMD (73).

SUPPLEMENTAL MATERIAL

Supplemental material for this article may be found at https://doi.org/10.1128/AEM .00823-18.

SUPPLEMENTAL FILE 1, PDF file, 0.9 MB.
SUPPLEMENTAL FILE 2, XLSX file, 0.1 MB.
SUPPLEMENTAL FILE 3, CSV file, 0.4 MB.
SUPPLEMENTAL FILE 4, XLSX file, 6.7 MB.
SUPPLEMENTAL FILE 5, CSV file, 14.5 MB.
SUPPLEMENTAL FILE 6, CSV file, 0.9 MB.
SUPPLEMENTAL FILE 7, CSV file, 0.3 MB.
SUPPLEMENTAL FILE 8, CSV file, 0.1 MB.

REFERENCES

1. Usui Y, Hirasawa T, Furusawa C, Shirai T, Yamamoto N, Mori H, Shimizu H. 2012. Investigating the effects of perturbations to *pgi* and *eno* gene expression on central carbon metabolism in Escherichia coli using ¹³C metabolic flux analysis. Microb Cell Fact 11:87. https://doi.org/10.1186/ 1475-2859-11-87.
2. Ahn J, Chung BKS, Lee D-Y, Park M, Karimi IA, Jung J-K, Lee H. 2011. NADPH-dependent *pgi*-gene knockout *Escherichia coli* metabolism producing shikimate on different carbon sources. FEMS Microbiol Lett 324:10–16. https://doi.org/10.1111/j.1574-6968.2011.02378.x.
3. Charusanti P, Conrad TM, Knight EM, Venkataraman K, Fong NL, Xie B, Gao Y, Palsson BØ. 2010. Genetic basis of growth adaptation of *Escherichia coli* after deletion of *pgi*, a major metabolic gene. PLoS Genet 6:e1001186. https://doi.org/10.1371/journal.pgen.1001186.
4. Fong SS, Nanchen A, Palsson BO, Sauer U. 2006. Latent pathway activation and increased pathway capacity enable Escherichia coli adaptation to loss of key metabolic enzymes. J Biol Chem 281:8024–8033. https:// doi.org/10.1074/jbc.M510016200.
5. Ishii N, Nakahigashi K, Baba T, Robert M, Soga T, Kanai A, Hirasawa T, Naba M, Hirai K, Hoque A, Ho PY, Kakazu Y, Sugawara K, Igarashi S, Harada S, Masuda T, Sugiyama N, Togashi T, Hasegawa M, Takai Y, Yugi

K, Arakawa K, Iwata N, Toya Y, Nakayama Y, Nishioka T, Shimizu K, Mori H, Tomita M. 2007. Multiple high-throughput analyses monitor the response of E. coli to perturbations. Science 316:593–597. https://doi.org/10.1126/science.1132067.

6. Richards GR, Patel MV, Lloyd CR, Vanderpool CK. 2013. Depletion of glycolytic intermediates plays a key role in glucose-phosphate stress in Escherichia coli. J Bacteriol 195:4816–4825. https://doi.org/10.1128/JB.00705-13.

7. Vanderpool CK, Gottesman S. 2004. Involvement of a novel transcriptional activator and small RNA in post-transcriptional regulation of the glucose phosphoenolpyruvate phosphotransferase system. Mol Microbiol 54:1076–1089. https://doi.org/10.1111/j.1365-2958.2004.04348.x.

8. Vanderpool CK, Gottesman S. 2007. The novel transcription factor SgrR coordinates the response to glucose-phosphate stress. J Bacteriol 189:2238–2248. https://doi.org/10.1128/JB.01689-06.

9. Holmgren A. 1976. Hydrogen donor system for Escherichia coli ribonucleoside-diphosphate reductase dependent upon glutathione. Proc Natl Acad Sci U S A 73:2275–2279.

10. Lin Z, Xu Z, Li Y, Wang Z, Chen T, Zhao X. 2014. Metabolic engineering of Escherichia coli for the production of riboflavin. Microb Cell Fact 13:104. https://doi.org/10.1186/s12934-014-0104-5.

11. Tenaillon O, Barrick JE, Ribeck N, Deatherage DE, Blanchard JL, Dasgupta A, Wu GC, Wielgoss S, Cruveiller S, Médigue C, Schneider D, Lenski RE. 2016. Tempo and mode of genome evolution in a 50,000-generation experiment. Nature 536:165–170. https://doi.org/10.1038/nature18959.

12. Plucain J, Hindré T, Le Gac M, Tenaillon O, Cruveiller S, Médigue C, Leiby N, Harcombe WR, Marx CJ, Lenski RE, Schneider D. 2014. Epistasis and allele specificity in the emergence of a stable polymorphism in Escherichia coli. Science 343:1366–1369. https://doi.org/10.1126/science.1248688.

13. Dragosits M, Mattanovich D. 2013. Adaptive laboratory evolution–principles and applications for biotechnology. Microb Cell Fact 12:64. https://doi.org/10.1186/1475-2859-12-64.

14. Chou H-H, Marx CJ, Sauer U. 2015. Transhydrogenase promotes the robustness and evolvability of E. coli deficient in NADPH production. PLoS Genet 11:e1005007. https://doi.org/10.1371/journal.pgen.1005007.

15. Nakahigashi K, Toya Y, Ishii N, Soga T, Hasegawa M, Watanabe H, Takai Y, Honma M, Mori H, Tomita M. 2009. Systematic phenome analysis of Escherichia coli multiple-knockout mutants reveals hidden reactions in central carbon metabolism. Mol Syst Biol 5:306. https://doi.org/10.1038/msb.2009.65.

16. LaCroix RA, Sandberg TE, O'Brien EJ, Utrilla J, Ebrahim A, Guzman GI, Szubin R, Palsson BO, Feist AM. 2015. Use of adaptive laboratory evolution to discover key mutations enabling rapid growth of Escherichia coli K-12 MG1655 on glucose minimal medium. Appl Environ Microbiol 81:17–30. https://doi.org/10.1128/AEM.02246-14.

17. Sandberg TE, Pedersen M, LaCroix RA, Ebrahim A, Bonde M, Herrgard MJ, Palsson BO, Sommer M, Feist AM. 2014. Evolution of Escherichia coli to 42°C and subsequent genetic engineering reveals adaptive mechanisms and novel mutations. Mol Biol Evol 31:2647–2662. https://doi.org/10.1093/molbev/msu209.

18. McCloskey D, Young JD, Xu S, Palsson BO, Feist AM. 2016. Modeling method for increased precision and scope of directly measurable fluxes at a genome-scale. Anal Chem 88:3844–3852. https://doi.org/10.1021/acs.analchem.5b04914.

19. Bak G, Lee J, Suk S, Kim D, Young Lee J, Kim K-S, Choi B-S, Lee Y. 2015. Identification of novel sRNAs involved in biofilm formation, motility, and fimbriae formation in Escherichia coli. Sci Rep 5:15287. https://doi.org/10.1038/srep15287.

20. Kimata K, Tanaka Y, Inada T, Aiba H. 2001. Expression of the glucose transporter gene, ptsG, is regulated at the mRNA degradation step in response to glycolytic flux in Escherichia coli. EMBO J 20:3587–3595. https://doi.org/10.1093/emboj/20.13.3587.

21. Vanderpool CK. 2007. Physiological consequences of small RNA-mediated regulation of glucose-phosphate stress. Curr Opin Microbiol 10:146–151. https://doi.org/10.1016/j.mib.2007.03.011.

22. Gama-Castro S, Salgado H, Santos-Zavaleta A, Ledezma-Tejeida D, Muñiz-Rascado L, García-Sotelo JS, Alquicira-Hernández K, Martínez-Flores I, Pannier L, Castro-Mondragón JA, Medina-Rivera A, Solano-Lira H, Bonavides-Martínez C, Pérez-Rueda E, Alquicira-Hernández S, Porrón-Sotelo L, López-Fuentes A, Hernández-Koutoucheva A, Del Moral-Chávez V, Rinaldi F, Collado-Vides J. 2016. RegulonDB version 9.0: high-level integration of gene regulation, coexpression, motif clustering and beyond. Nucleic Acids Res 44:D133–D143. https://doi.org/10.1093/nar/gkv1156.

23. Cho S, Cho Y-B, Kang TJ, Kim SC, Palsson B, Cho B-K. 2015. The architecture of ArgR-DNA complexes at the genome-scale in Escherichia coli. Nucleic Acids Res 43:3079–3088. https://doi.org/10.1093/nar/gkv150.

24. Federowicz S, Kim D, Ebrahim A, Lerman J, Nagarajan H, Cho B-K, Zengler K, Palsson B. 2014. Determining the control circuitry of redox metabolism at the genome-scale. PLoS Genet 10:e1004264. https://doi.org/10.1371/journal.pgen.1004264.

25. Kim D, Hong JS-J, Qiu Y, Nagarajan H, Seo J-H, Cho B-K, Tsai S-F, Palsson BØ. 2012. Comparative analysis of regulatory elements between Escherichia coli and Klebsiella pneumoniae by genome-wide transcription start site profiling. PLoS Genet 8:e1002867. https://doi.org/10.1371/journal.pgen.1002867.

26. Cho B-K, Federowicz S, Park Y-S, Zengler K, Palsson BØ. 2011. Deciphering the transcriptional regulatory logic of amino acid metabolism. Nat Chem Biol 8:65–71. https://doi.org/10.1038/nchembio.710.

27. Larson TJ, Cantwell JS, van Loo-Bhattacharya AT. 1992. Interaction at a distance between multiple operators controls the adjacent, divergently transcribed glpTQ-glpACB operons of Escherichia coli K-12. J Biol Chem 267:6114–6121.

28. Weston LA, Kadner RJ. 1988. Role of uhp genes in expression of the Escherichia coli sugar-phosphate transport system. J Bacteriol 170:3375–3383. https://doi.org/10.1128/jb.170.8.3375-3383.1988.

29. Dahl JL, Wei BY, Kadner RJ. 1997. Protein phosphorylation affects binding of the Escherichia coli transcription activator UhpA to the uhpT promoter. J Biol Chem 272:1910–1919. https://doi.org/10.1074/jbc.272.3.1910.

30. Maloney PC, Ambudkar SV, Anatharam V, Sonna LA, Varadhachary A. 1990. Anion-exchange mechanisms in bacteria. Microbiol Rev 54:1–17.

31. Bolten CJ, Kiefer P, Letisse F, Portais J-C, Wittmann C. 2007. Sampling for metabolome analysis of microorganisms. Anal Chem 79:3843–3849. https://doi.org/10.1021/ac0623888.

32. Link H, Anselment B, Weuster-Botz D. 2008. Leakage of adenylates during cold methanol/glycerol quenching of Escherichia coli. Metabolomics 4:240–247. https://doi.org/10.1007/s11306-008-0114-6.

33. Stoebel DM, Dean AM, Dykhuizen DE. 2008. The cost of expression of Escherichia coli lac operon proteins is in the process, not in the products. Genetics 178:1653–1660. https://doi.org/10.1534/genetics.107.085399.

34. Kaleta C, Schäuble S, Rinas U, Schuster S. 2013. Metabolic costs of amino acid and protein production in Escherichia coli. Biotechnol J 8:1105–1114. https://doi.org/10.1002/biot.201200267.

35. Traxler MF, Chang D-E, Conway T. 2006. Guanosine 3',5'-bispyrophosphate coordinates global gene expression during glucose-lactose diauxie in Escherichia coli. Proc Natl Acad Sci U S A 103:2374–2379. https://doi.org/10.1073/pnas.0510995103.

36. Tao H, Bausch C, Richmond C, Blattner FR, Conway T. 1999. Functional genomics: expression analysis of Escherichia coli growing on minimal and rich media. J Bacteriol 181:6425–6440.

37. Akashi H, Gojobori T. 2002. Metabolic efficiency and amino acid composition in the proteomes of Escherichia coli and Bacillus subtilis. Proc Natl Acad Sci U S A 99:3695–3700. https://doi.org/10.1073/pnas.062526999.

38. Weickert MJ, Adhya S. 1993. The galactose regulon of Escherichia coli. Mol Microbiol 10:245–251. https://doi.org/10.1111/j.1365-2958.1993.tb01950.x.

39. Schlegel A, Böhm A, Lee S-J, Peist R, Decker K, Boos W. 2002. Network regulation of the Escherichia coli maltose system. J Mol Microbiol Biotechnol 4:301–307.

40. Liu P, Danot O, Richet E. 2013. A dual role for the inducer in signalling by MalT, a signal transduction ATPase with numerous domains (STAND). Mol Microbiol 90:1309–1323. https://doi.org/10.1111/mmi.12434.

41. Danot O. 2010. The inducer maltotriose binds in the central cavity of the tetratricopeptide-like sensor domain of MalT, a bacterial STAND transcription factor. Mol Microbiol 77:628–641. https://doi.org/10.1111/j.1365-2958.2010.07237.x.

42. McCloskey D, Gangoiti JA, Palsson BO, Feist AM. 2015. A pH and solvent optimized reverse-phase ion-paring-LC-MS/MS method that leverages multiple scan-types for targeted absolute quantification of intracellular metabolites. Metabolomics 11:1338–1350. https://doi.org/10.1007/s11306-015-0790-y.

43. Gaudu P, Weiss B. 1996. SoxR, a [2Fe-2S] transcription factor, is active only in its oxidized form. Proc Natl Acad Sci U S A 93:10094–10098.

44. Bradley TM, Hidalgo E, Leautaud V, Ding H, Demple B. 1997. Cysteine-to-alanine replacements in the Escherichia coli SoxR protein and the role

of the [2Fe-2S] centers in transcriptional activation. Nucleic Acids Res 25:1469–1475. https://doi.org/10.1093/nar/25.8.1469.

45. Tseng C-P, Yu C-C, Lin H-H, Chang C-Y, Kuo J-T. 2001. Oxygen- and growth rate-dependent regulation of Escherichia coli fumarase (FumA, FumB, and FumC) activity. J Bacteriol 183:461–467. https://doi.org/10.1128/JB.183.2.461-467.2001.

46. Koo M-S, Lee J-H, Rah S-Y, Yeo W-S, Lee J-W, Lee K-L, Koh Y-S, Kang S-O, Roe J-H. 2003. A reducing system of the superoxide sensor SoxR in Escherichia coli. EMBO J 22:2614–2622. https://doi.org/10.1093/emboj/cdg252.

47. Canonaco F, Hess TA, Heri S, Wang T, Szyperski T, Sauer U. 2001. Metabolic flux response to phosphoglucose isomerase knock-out in Escherichia coli and impact of overexpression of the soluble transhydrogenase UdhA. FEMS Microbiol Lett 204:247–252. https://doi.org/10.1111/j.1574-6968.2001.tb10892.x.

48. Sauer U, Canonaco F, Heri S, Perrenoud A, Fischer E. 2004. The soluble and membrane-bound transhydrogenases UdhA and PntAB have divergent functions in NADPH metabolism of Escherichia coli. J Biol Chem 279:6613–6619. https://doi.org/10.1074/jbc.M311657200.

49. Walsh K, Koshland DE, Jr. 1985. Branch point control by the phosphorylation state of isocitrate dehydrogenase. A quantitative examination of fluxes during a regulatory transition. J Biol Chem 260:8430–8437.

50. McKee JS, Nimmo HG. 1989. Evidence for an arginine residue at the coenzyme-binding site of Escherichia coli isocitrate dehydrogenase. Biochem J 261:301–304. https://doi.org/10.1042/bj2610301.

51. LaPorte DC, Walsh K, Koshland DE, Jr. 1984. The branch point effect. Ultrasensitivity and subsensitivity to metabolic control. J Biol Chem 259:14068–14075.

52. Zhu G, Golding GB, Dean AM. 2005. The selective cause of an ancient adaptation. Science 307:1279–1282. https://doi.org/10.1126/science.1106974.

53. Datsenko KA, Wanner BL. 2000. One-step inactivation of chromosomal genes in Escherichia coli K-12 using PCR products. Proc Natl Acad Sci U S A 97:6640–6645. https://doi.org/10.1073/pnas.120163297.

54. Sambrook J, Russell DW. 2001. Molecular cloning: a laboratory manual, 3rd ed. Cold Spring Harbor Laboratory Press, Cold Spring Harbor, NY.

55. Fong SS, Burgard AP, Herring CD, Knight EM, Blattner FR, Maranas CD, Palsson BO. 2005. In silico design and adaptive evolution of Escherichia coli for production of lactic acid. Biotechnol Bioeng 91:643–648. https://doi.org/10.1002/bit.20542.

56. Orth JD, Conrad TM, Na J, Lerman JA, Nam H, Feist AM, Palsson BØ. 2011. A comprehensive genome-scale reconstruction of Escherichia coli metabolism–2011. Mol Syst Biol 7:535. https://doi.org/10.1038/msb.2011.65.

57. Schellenberger J, Palsson BØ. 2009. Use of randomized sampling for analysis of metabolic networks. J Biol Chem 284:5457–5461. https://doi.org/10.1074/jbc.R800048200.

58. McCloskey D, Young JD, Xu S, Palsson BO, Feist AM. 2016. MID Max: LC-MS/MS method for measuring the precursor and product mass isotopomer distributions of metabolic intermediates and cofactors for metabolic flux analysis applications. Anal Chem 88:1362–1370. https://doi.org/10.1021/acs.analchem.5b03887.

59. McCloskey D, Gangoiti JA, King ZA, Naviaux RK, Barshop BA, Palsson BO, Feist AM. 2014. A model-driven quantitative metabolomics analysis of aerobic and anaerobic metabolism in E. coli K-12 MG1655 that is biochemically and thermodynamically consistent. Biotechnol Bioeng 111:803–815. https://doi.org/10.1002/bit.25133.

60. McCloskey D, Utrilla J, Naviaux RK, Palsson BO, Feist AM. 2014. Fast Swinnex filtration (FSF): a fast and robust sampling and extraction method suitable for metabolomics analysis of cultures grown in complex media. Metabolomics 11:198–209. https://doi.org/10.1007/s11306-014-0686-2.

61. Honaker J, King G, Blackwell M. 2011. Amelia II: a program for missing data. J Stat Softw 45:1–47.

62. Rocke D, Tillinghast J, Durbin-Johnson B, Wu SL. 2013. LMGene software for data transformation and identification of differentially expressed genes in gene expression arrays. R package version 2.4.0.

63. Young JD. 2014. INCA: a computational platform for isotopically nonstationary metabolic flux analysis. Bioinformatics 30:1333–1335. https://doi.org/10.1093/bioinformatics/btu015.

64. Megchelenbrink W, Huynen M, Marchiori E. 2014. optGpSampler: an improved tool for uniformly sampling the solution-space of genome-scale metabolic networks. PLoS One 9:e86587. https://doi.org/10.1371/journal.pone.0086587.

65. Langmead B, Trapnell C, Pop M, Salzberg SL. 2009. Ultrafast memory-efficient short read aligner. Genome Biol 10:R25. https://doi.org/10.1186/gb-2009-10-3-r25.

66. Trapnell C, Williams BA, Pertea G, Mortazavi A, Kwan G, van Baren MJ, Salzberg SL, Wold BJ, Pachter L. 2010. Transcript assembly and quantification by RNA-Seq reveals unannotated transcripts and isoform switching during cell differentiation. Nat Biotechnol 28:511–515. https://doi.org/10.1038/nbt.1621.

67. Deatherage DE, Barrick JE. 2014. Identification of mutations in laboratory-evolved microbes from next-generation sequencing data using breseq. Methods Mol Biol 1151:165–188. https://doi.org/10.1007/978-1-4939-0554-6_12.

68. Berman HM, Westbrook J, Feng Z, Gilliland G, Bhat TN, Weissig H, Shindyalov IN, Bourne PE. 2000. The Protein Data Bank. Nucleic Acids Res 28:235–242. https://doi.org/10.1093/nar/28.1.235.

69. Berman H, Henrick K, Nakamura H. 2003. Announcing the worldwide Protein Data Bank. Nat Struct Biol 10:980. https://doi.org/10.1038/nsb1203-980.

70. Xu D, Zhang Y. 2013. Ab initio structure prediction for Escherichia coli: towards genome-wide protein structure modeling and fold assignment. Sci Rep 3:1895. https://doi.org/10.1038/srep01895.

71. Wu S, Skolnick J, Zhang Y. 2007. Ab initio modeling of small proteins by iterative TASSER simulations. BMC Biol 5:17. https://doi.org/10.1186/1741-7007-5-17.

72. Keseler IM, Mackie A, Peralta-Gil M, Santos-Zavaleta A, Gama-Castro S, Bonavides-Martínez C, Fulcher C, Huerta AM, Kothari A, Krummenacker M, Latendresse M, Muñiz-Rascado L, Ong Q, Paley S, Schröder I, Shearer AG, Subhraveti P, Travers M, Weerasinghe D, Weiss V, Collado-Vides J, Gunsalus RP, Paulsen I, Karp PD. 2013. EcoCyc: fusing model organism databases with systems biology. Nucleic Acids Res 41:D605–D612. https://doi.org/10.1093/nar/gks1027.

73. Humphrey W, Dalke A, Schulten K. 1996. VMD: visual molecular dynamics. J Mol Graph 14:33–38. https://doi.org/10.1016/0263-7855(96)00018-5.

74. Sun Y, Vanderpool CK. 2013. Physiological consequences of multiple-target regulation by the small RNA SgrS in Escherichia coli. J Bacteriol 195:4804–4815. https://doi.org/10.1128/JB.00722-13.

75. Bobrovskyy M, Vanderpool CK. 2016. Diverse mechanisms of post-transcriptional repression by the small RNA regulator of glucose-phosphate stress. Mol Microbiol 99:254–273. https://doi.org/10.1111/mmi.13230.

76. Geanacopoulos M, Adhya S. 1997. Functional characterization of roles of GalR and GalS as regulators of the gal regulon. J Bacteriol 179:228–234. https://doi.org/10.1128/jb.179.1.228-234.1997.

77. Aki T, Adhya S. 1997. Repressor induced site-specific binding of HU for transcriptional regulation. EMBO J 16:3666–3674. https://doi.org/10.1093/emboj/16.12.3666.

78. Semsey S, Krishna S, Sneppen K, Adhya S. 2007. Signal integration in the galactose network of Escherichia coli. Mol Microbiol 65:465–476. https://doi.org/10.1111/j.1365-2958.2007.05798.x.

79. Liochev SI, Fridovich I. 2011. Is superoxide able to induce SoxRS? Free Radic Biol Med 50:1813. https://doi.org/10.1016/j.freeradbiomed.2011.03.029.

80. Lo F-C, Lee J-F, Liaw W-F, Hsu I-J, Tsai Y-F, Chan SI, Yu SS-F. 2012. The metal core structures in the recombinant Escherichia coli transcriptional factor SoxR. Chemistry 18:2565–2577. https://doi.org/10.1002/chem.201100838.

81. Kobayashi K. 2017. Sensing mechanisms in the redox-regulated, [2Fe-2S] cluster-containing, bacterial transcriptional factor SoxR. Acc Chem Res 50:1672–1678. https://doi.org/10.1021/acs.accounts.7b00137.

82. Ding H, Demple B. 1996. Glutathione-mediated destabilization in vitro of [2Fe-2S] centers in the SoxR regulatory protein. Proc Natl Acad Sci U S A 93:9449–9453.

83. Hidalgo E, Demple B. 1994. An iron-sulfur center essential for transcriptional activation by the redox-sensing SoxR protein. EMBO J 13:138–146.

84. Hidalgo E, Bollinger JM, Jr, Bradley TM, Walsh CT, Demple B. 1995. Binuclear [2Fe-2S] clusters in the Escherichia coli SoxR protein and role of the metal centers in transcription. J Biol Chem 270:20908–20914. https://doi.org/10.1074/jbc.270.36.20908.

85. Hidalgo E, Demple B. 1996. Activation of SoxR-dependent transcription in vitro by noncatalytic or NifS-mediated assembly of [2Fe-2S] clusters into apo-SoxR. J Biol Chem 271:7269–7272. https://doi.org/10.1074/jbc.271.13.7269.

86. Watanabe S, Kita A, Kobayashi K, Miki K. 2008. Crystal structure of the [2Fe-2S] oxidative-stress sensor SoxR bound to DNA. Proc Natl Acad Sci U S A 105:4121–4126. https://doi.org/10.1073/pnas.0709188105.